Exploring the Energy Storage Mechanism of High Performance MnO$_2$ Electrochemical Capacitor Electrodes: An In Situ Atomic Force Microscopy Study in Aqueous Electrolyte

Xinyong Tao, Jun Du, Yong Sun, Shulan Zhou, Yang Xia, Hui Huang, Yongping Gan, Wenkui Zhang,* and Xiaodong Li**

The basic microstructure-dependent charge storage mechanisms of nanostructured MnO$_2$ are investigated via dynamic observation of the growth and in situ probing the mechanical properties by using in situ AFM in conjunction with in situ nanoindentation. The progressive nucleation followed by three-dimensional growth yields pulsed current deposited porous nanostructured γ-MnO$_2$, which exhibits a high specific capacitance of 437 F/g and a remarkable cycling performance with >96% capacitance retention after 10 000 cycles. The proton intercalation induced expansion of MnO$_2$ can be self-accommodated by the localized compression and reduction of the porosity. More coincidentally, the proton intercalation induced softening is favorable for the elastic deformation of MnO$_2$. This self-adaptive capability of nanostructured MnO$_2$ could generate high structural reliability during cycling. These discoveries offer important mechanistic insights for the design of advanced electrochemical capacitors.

1. Introduction

Electrochemical capacitors,[1–5] with a super high power density, are promising energy storage devices that bridge the gap between batteries and conventional capacitors. Pseudocapacitive metal oxides (e.g., oxides of Mn, Ru, Fe, Co, Ni, Cr, Mo, W, V, etc.)[5–7] have been studied extensively as electrode materials for electrochemical capacitors owing to their high energy density and large faradic pseudocapacitance which is based on fast and reversible redox reactions in electrodes, resulting in much higher specific capacitance exceeding that of carboneous materials using electric double layer charge storage. Although MnO$_2$ is considered the most promising electrode material due to its low cost, sufficiently high theoretical specific capacitance (1370 F g^{-1}), environmental amiability, and natural abundance, the poor conductivity (10^{-5}–10^{-6} S cm^{-1}) of MnO$_2$ limits the rate capability for high power applications.[8–10]

To improve the electrical conductivity for optimizing the electrochemical properties of MnO$_2$, considerable research efforts have been placed on designing state-of-the-art electrodes. Under intense scrutiny for two decades, nearly all of strategies can be classified into one general concept, that is, constructing nanostructured MnO$_2$-conductive matrix hybrid electrodes.[6,10–30] Many recent reports demonstrated that high performance can be obtained from nanostructured MnO$_2$ films grown on highly conductive substrates such as metal nanostructures,[6,19] carbon nanotubes (CNT),[10,17,18] graphene,[14,15,25] and conducting polymers.[16,27] Hou et al. synthesized MnO$_2$/CNT/conducting polymer ternary electrodes exhibiting a specific capacitance of 427 F/g.[24] Lang et al. developed a nanoporous Au/MnO$_2$ film electrode via the combination of chemical de-alloying and electroless plating, resulting in a specific capacitance of ≈1145 F g^{-1} which is close to the theoretical value.[6] Chen et al. demonstrated an electrodeposited MnO$_2$ nanofilm on the CNT-sponge matrix with a specific capacitance of 1230 F g^{-1} and only 4% of degradation after 10 000 cycles.[10] Donne et al. grew the electrodeposited MnO$_2$ film with a significantly high capacitance over 2000 F g^{-1}, which resulted from the hydroxyl groups on the surface.[31] However, most of the research efforts focused on MnO$_2$ compounds with a target to achieve high cyclability and capacitance. Surprisingly, the basic microstructure-dependent charge storage mechanisms of nanostructured MnO$_2$ have been overlooked. A fundamental understanding of the

---

Prof. X. Y. Tao, Dr. J. Du, Y. Xia, Prof. H. Huang,
Y. P. Gan, W. K. Zhang
College of Chemical Engineering and Materials Science
Zhejiang University of Technology
Hangzhou, 310014, China
E-mail: tao@zjut.edu.cn; msechem@zjut.edu.cn

Dr. Y. Sun, Prof. X. D. Li
Department of Mechanical Engineering
University of South Carolina
300 Main Street, Columbia, SC 29208, USA
E-mail: lixiao@cec.sc.edu

Dr. S. L. Zhou
Department of Materials Science and Engineering
Jingdezhen Ceramics Institute
Jingdezhen, 333403, China

DOI: 10.1002/adfm.201300359

microstructure and how it correlates with charge storage are essential in optimizing the final microstructure of MnO_2.

Ex situ X-ray photoelectron spectroscopy (XPS),[9] in situ X-ray diffraction (XRD)[9] and in situ X-ray absorption spectroscopy (XAS)[32] have been developed to monitor the structural breathing of MnO_2 during cycling. The preparation and the subsequent electrochemical energy storage of MnO_2 generally involve liquid-phase processes. Imaging of the samples in liquid via transmission electron microscopy (TEM),[33–36] scanning electron microscopy (SEM)[35] and atomic force microscopy (AFM)[37] can provide unique insights into biological systems, such as cells containing labelled proteins,[35] and into processes of importance in materials science, such as solution-phase nanoparticle growth[33,34] and electrochemical reactions.[36,37] Here we analyse dynamic observations—recorded in situ using a liquid AFM technique—of the growth mechanisms of nanoscale MnO_2 clusters with remarkable energy-storage performance. Moreover, coupled in situ nanoindentation and first-principles density function theory (DFT) was used to uncover the energy storage mechanism of nanostructured MnO_2. A series of dramatic evolutions of nanostructured MnO_2 film involving progressive nucleation, three dimensional growth, reversible expansion, proton intercalation induced softening, and self-accommodation phenomena can be correlated to its remarkable energy storage performance. Our observations offer important mechanistic insights for the design of advanced electrochemical capacitors.

2. Results and Discussion

We have successfully constructed a facile and novel electrochemical device consisting of a platinum film as the counter electrode, Ag/AgCl microelectrode as the reference electrode, ITO film as the conductive substrate for nanostructured MnO_2 films (Supporting Information Figure S1a). A key feature of this micro-device is to enable the direct real-time visualization of both the MnO_2 growth and the pseudocapacitive redox reaction induced microstructural and mechanical changes of the same MnO_2 sample on the same working platform. Electrochemical deposition is one of the most attractive methods for the synthesis of thin MnO_2 films.[16,19,27,38] However, the formation mechanism under various electrodeposition conditions is still, to a large extent, unknown. The lack of consensus on the deposition mechanisms is mainly due to the absence of direct experimental evidence for film growth in solution. Correspondingly, in situ observation of the dynamic growth process is expected to substantially advance our understanding of nanostructured MnO_2 film growth. **Figure 1** shows the in situ AFM observation of the nucleation and growth of the pulsed current deposited MnO_2 film on ITO substrate in aqueous electrolyte taken from the same field of view. Only a few ITO nanocrystals can be found in the AFM image of the original ITO electrode (Figure 1a). Abundant nuclei appear after 10 s electrodeposition (Figure 1b). Generally, the microstructure of MnO_2 depends on electrokinetic phenomena during the synthesis process. It is postulated that oxidation of Mn^{2+} to MnO_2 occurs following the reaction below:[39,40]

$$Mn^{2+} + 4OH^- \rightarrow MnO_2 + 2H_2O + 2e^- \quad (1)$$

The electrodeposition process can be controlled via two fundamental electrokinetic phenomena, i.e., nucleation and growth of crystal grains. There are usually two kinds of nucleation mechanisms, the instantaneous and the progressive. In the instantaneous nucleation mechanism, all nuclei are rapidly created during the first stages and their number remains constant throughout growth. In the progressive nucleation mechanism,

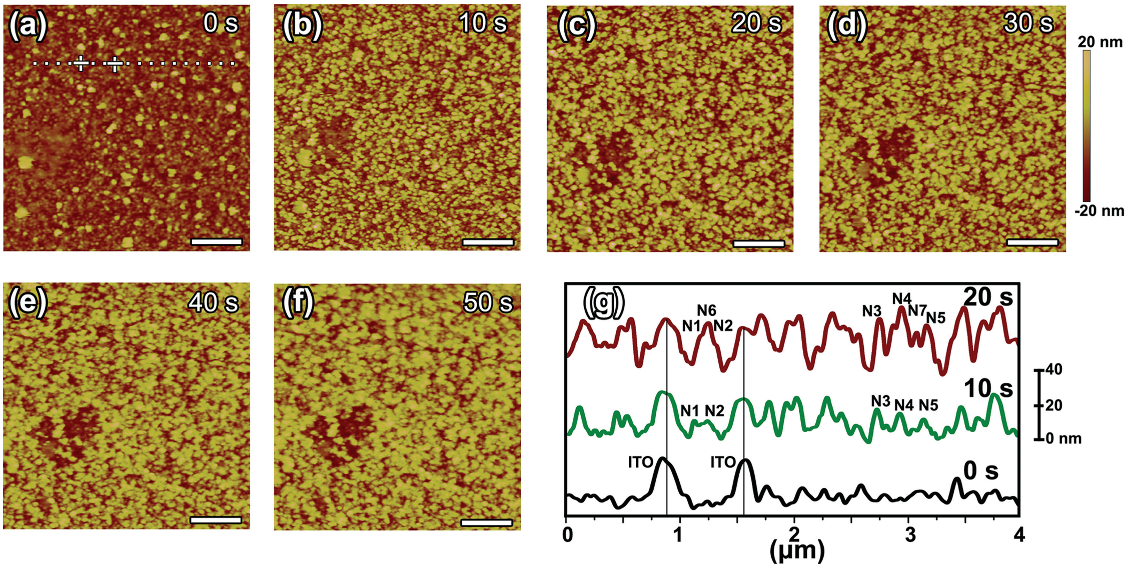

Figure 1. In situ AFM observation of the nucleation and growth of the MnO_2 nanofilm electrochemically deposited on tin-doped indium oxide (ITO) electrode in aqueous electrolyte. a) AFM image of the original ITO electrode. b–f) Real-time in situ AFM images of MnO_2 nanofilm. g) Cross sectional AFM profiles showing nucleation and growth trajectories. Scale bar 1 µm.

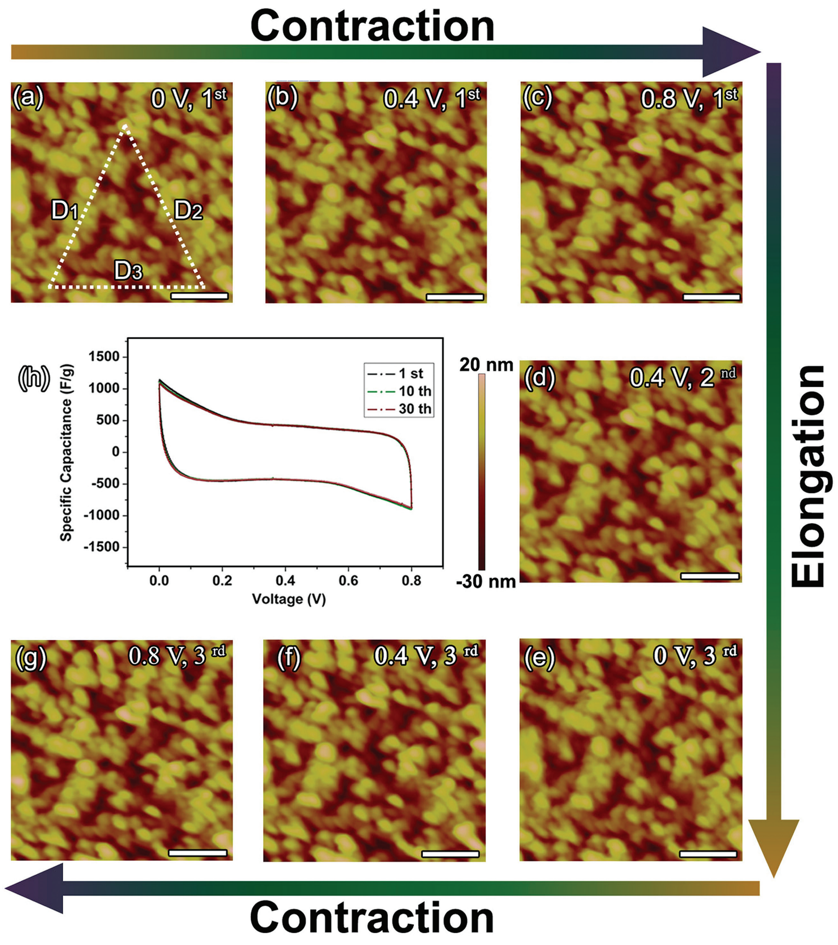

Figure 2. In situ AFM observation of the microstructural evolution during charging and discharging processes in aqueous electrolyte. a–g) In situ AFM images recorded at different applied potentials vs. Ag/AgCl. h) Representative CV curves of the electrodeposited MnO_2 for the 1st, 10th, and 30th cycles in 0.1 M aqueous electrolyte. Scale bar: 500 nm.

new nuclei are continuously formed during the whole electrodeposition process because the nucleation rate process is low. Compared with the AFM image (Figure 1b) obtained after 10 s electrodeposition, more nuclei can be found after 20–50 s deposition (Figure 1c–f), suggesting that progressive nucleation mechanism is predominant in this case. Figure 1g reveals the cross sectional AFM height-profile showing nucleation and growth trajectories. Two apparent nuclei (N1 and N2) between the two ITO nanoparticles can be found after 10s electrodeposition (Figure 1g). The AFM profile corresponding to 20 s growth reveals the increase in the diameter of N1 and N2, indicating the three-dimensional (3D) growth of MnO_2 nuclei. The merging of nuclei of N1 and N2 can also be observed (Figure 1g). Some new nuclei such as N6 and N7 appear after 20 s growth, indicating the progressive nucleation clearly. A continuous porous coating with the average thickness of 59 nm can be obtained after 50 s electrodeposition, which was constructed by MnO_2 nanoparticles (Figure 1f). It is notable that large amounts of interparticle mesopores are formed, which can provide a more favorable path for electrolyte penetration and transportation. Average growth rate of 1.16 nm/s was extracted from the in situ AFM measurement. XRD patterns (Supporting Information Figure S2) and high resolution transmission electron microscopy (HRTEM) images (Supporting Information Figure S3) jointly prove that the nanostructured film is polycrystalline γ-MnO_2.

After the in situ growth of MnO_2 film, 1 M KCl aqueous electrolyte was used for the cyclic voltammetry (CV) test combined with in situ AFM observation. **Figure 2** reveals the in situ AFM observation of the microstructural evolution during charging and discharging processes in aqueous electrolyte. Figure 2h displays the representative CV curves for the 1st, 10th, and 30th cycles. This nanostructured MnO_2 film exhibited a high specific capacitance of 437 F/g. Figure 2a–g show the in situ AFM images recorded at different applied potentials. To identify the microstructural changes during the cycling, the interparticle distances (D_1, D_2, and D_3) between 3 typical nanoparticles in Figure 2a–g were measured via in situ AFM observation. **Table 1** reveals the distance variation of D_1, D_2 and D_3 at different voltages. Obvious contraction/extension of D_1 and D_2 can be found during the corresponding charging/discharging processes. The maximum/minimum interparticle distances appear at 0/0.8 V, respectively. This reversible elongation/contraction must result from the periodic deformation of nanoparticles. However, no distinct grain rotation can be observed in the in situ AFM measurement, implying that the periodic elongation/contraction may come from the reversible volumetric shrinkage and swelling during the cycling.

The nanostructured MnO_2 showed good cycle stability with extremely low fading rate of specific capacitance after 30 cycles (Figure 2h). **Figure 3**a,b show the in situ AFM images recorded at 0.8 and 0 V after 30 cycles, respectively. Compared with the AFM images in Figure 2, no obvious evolution can be observed in the number, the location, the orientation and the morphology of the MnO_2 nanoparticles in the same area, revealing the high structural reliability of nanostructured MnO_2 during the charging and discharging processes. In order to investigate whether there was grain expansion during the discharging process, AFM height profiles (Figure 3c) corresponding to an identical area at 0.8 and 0 V in the exact same locations were

Table 1. Variation of the interparticle distance between three typical nanoparticles at different voltages.

	0 V 1st	0.4V 1st	0.8 V 1st	0.4V 2nd	0 V 2nd	0.4V 3rd	0.8 V 3rd
D_1 [nm]	1571	↓1503	↓1446	↑1509	↑1572	↓1479	↓1443
D_2 [nm]	1586	↓1541	↓1503	↑1554	↑1591	↓1537	↓1498
D_3 [nm]	1420	↓1415	↓1399	↑1418	↑1429	↓1417	↓1403

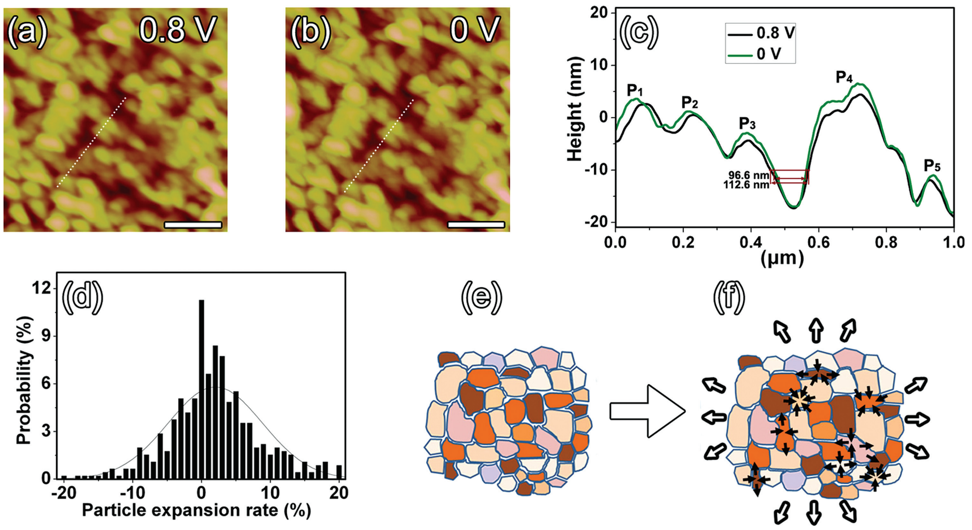

Figure 3. Charge/discharge induced expansion and contraction of the MnO_2 nanoparticles. a) AFM image recorded at 0.8 V. b) AFM image recorded at 0 V. c) Detailed comparison of height profiles at 0 and 0.8 V. d) Statistical chart of the discharge induced expansion rate based on more than 200 grains. e–f) Deformation mechanism of the nanostructured MnO_2 film during the discharge process. Scale bar 500 nm.

used to investigate the detailed deformation mechanism. The noticeable expansion in height can be observed in grains P_3 and P_4. Apparent elongation of the interparticle distance between grains P_1 and P_4 can be attributed to the particle expansion during the discharging process. Although similar expansion can also be found in grain P5, a little detectable compression can be identified in grain P_5 along x-axis direction.

More intriguingly, the diameter of interparticle pore between P_3 and P_4 contracted from 112.6 to 96.6 nm during the discharging process, indicating that the expansion of nanoparticles can be accommodated by the shrinkage of interparticle pores. Height profiles of more than 200 grains on the images were measured carefully with similar routine. The overall results are listed in a bar chart (Figure 3d). From the bar chart, it is clear that the grains went through a dominant expansion process, as implied by the positive average expansion rate of 1.9% by averaging values on all directions. The bar chart also confirms that a considerable number of grains shrank instead of going through homogeneous expansion. Such localized compression is understandable, as to compromise the expansion of adjacent grains in some cases. A cartoon is sketched in Figure 3e,f in order to briefly represent this inhomogeneous procedure. This kind of expansion must be related to the faradic redox reactions during the energy storage process. There are two mechanisms proposed to explain the MnO_2 charge storage behavior. The first one implies the intercalation of protons (H^+) or alkali metal cations (C^+) such as Li^+ in the bulk of MnO_2 upon reduction followed by deintercalation upon oxidation:[9]

$$MnO_2 + H^+ + e^- \leftrightarrow MnOOH \qquad (2)$$

or

$$MnO_2 + C^+ + e^- \leftrightarrow MnOOC \qquad (3)$$

The second mechanism is based on the surface adsorption of electrolyte cations (C^+) on MnO_2:[9]

$$(MnO_2)_{surface} + C^+ + e^- \leftrightarrow (MnO_2 - C^+)_{surface} \qquad (4)$$

where $C^+ = Li^+, Na^+, K^+$. Donne et al. clarified that metals larger than H^+ and Li^+ cannot to any great extent be inserted into the manganese dioxide structure due to size effects.[31] Our ex situ XPS results (Supporting Information Figure S4) also revealed that the K/Mn ratio for the reduced electrode was much lower than what was anticipated for charge compensation dominated by K^+, suggesting that the proton plays the absolute predominant role in the pseudofaradaic mechanism. Therefore, the expansion observed by in situ AFM can be attributed to the proton intercalation induced lattice expansion and the change of ionic radii of Mn species in MnO_2 during discharge. The size of Mn species increases significantly from their 4+ oxidation state (0.530 Å) to 3+ oxidation state (0.645 Å). This proton intercalation induced expansion would lead to a shifting of the particle to particle contact points and thus reforming of the established porous electrode matrix. Since the nanostructured MnO_2 film possesses unique porous structure as shown in Figures 1–3, the expansion of particles can be compromised by localized compression and accommodated by reducing the porosity of the electrode, which has been unveiled by in situ AFM observations (Figure 3). This self-adaptive capability of nanostructured MnO_2 could generate high structural reliability during the charging and discharging. The nanostructured MnO_2 exhibited a remarkable cycling performance with >96% capacitance retention after 10 000 cycles (Supporting Information Figure S5).

Nanostructured MnO_2 films and coatings especially in highly flexible electrochemical capacitor devices will undergo large and repeated stretches, bends and twists.[10–12,18,20,41] Fabrication of mechanically robust nanostructured MnO_2 requires a basic understanding of the mechanical properties during service. However, the detailed mechanism of mechanical property evolution of MnO_2 film in the charge/discharge process is largely unknown due to the challenges for achieving in situ

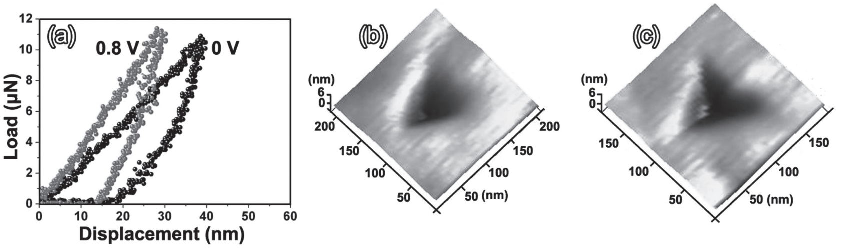

Figure 4. In situ nanoindentation of the MnO_2 nanofilm probing the mechanical property evolution during the energy storage process. a) Representative load-displacement curves with a peak load of 11 μN at 0.8 and 0 V vs Ag/AgCl. b,c) Representative AFM images of the indentation impression made on MnO_2 with a peak load of 11 μN at 0.8 and 0 V, respectively.

mechanical tests. Nanoindentation has been proven a powerful method for in situ probing the mechanical properties of nanostructures in our previous work.[42–44] Here, the electrochemical device (Figure S1a) enables the in situ nanoindentation on the MnO_2 film in addition to the in situ observation of nucleation, growth and morphological changes. **Figure 4**a shows the representative load-displacement curves with a peak load of 11 μN at 0.8 and 0 V. The loading curves without discontinuities or steps indicate that no cracks were formed during indentation. There is no apparent plastic pile-up in the AFM image of the indentation impression (Figure 4b,c) under a peak load of 11 μN, promising that Oliver and Pharr method[42–44] can be adopted to extract the mechanical properties of the MnO_2 film. The elastic modulus of the MnO_2 film at 0.8 and 0 V were measured to be 54.5 ± 4.9 and 39.8 ± 2.3 GPa, respectively, obtained from twenty nanoindentation tests. The nanoindentation hardness values at 0.8 and 0V were measured to be 1.2 ± 0.2 and 1.0 ± 0.1 GPa, respectively. A 27% reduction in elastic modulus and a 20% reduction in hardness can be found after the discharging process, revealing an evident proton intercalation induced softening.

In order to elucidate the effect of proton intercalation on mechanical properties and geometrical structures, we conducted first-principles calculations of MnO_2 using the Cambridge Sequential Total Energy Code (CASTEP). The structure of γ-MnO_2 is composed of an intergrowth of ramsdellite (R-MnO_2, space group *Pbnm*) and pyrolusite (β-MnO_2, space group $P4_2/mnm$) and can be parameterized by P_r, as defined by Chabre and Pannetier,[45] which represents the fraction of pyrolusite domains in a ramsdellite-based structure. The range of P_r for γ-MnO_2 samples prepared by electrochemical deposition varies from 40% to 60%.[45] Chabre and Pannetier stated that pyrolusite contains only one type of oxygen atom, whereas ramsdellite contains two symmetry-inequivalent bonding angles which make with their Mn neighbors.[45] Since the types of oxygen atoms (pyramidal and planar) distinguished by the two oxygens are at different lattice potentials (planar oxygen is less stabilized by the lattice potential), pyramidal oxygen is more likely to be hydroxylated than planar oxygen.[45,46] **Figure 5**a,b illustrate the proton intercalation induced change in electron density distribution of R-MnO_2

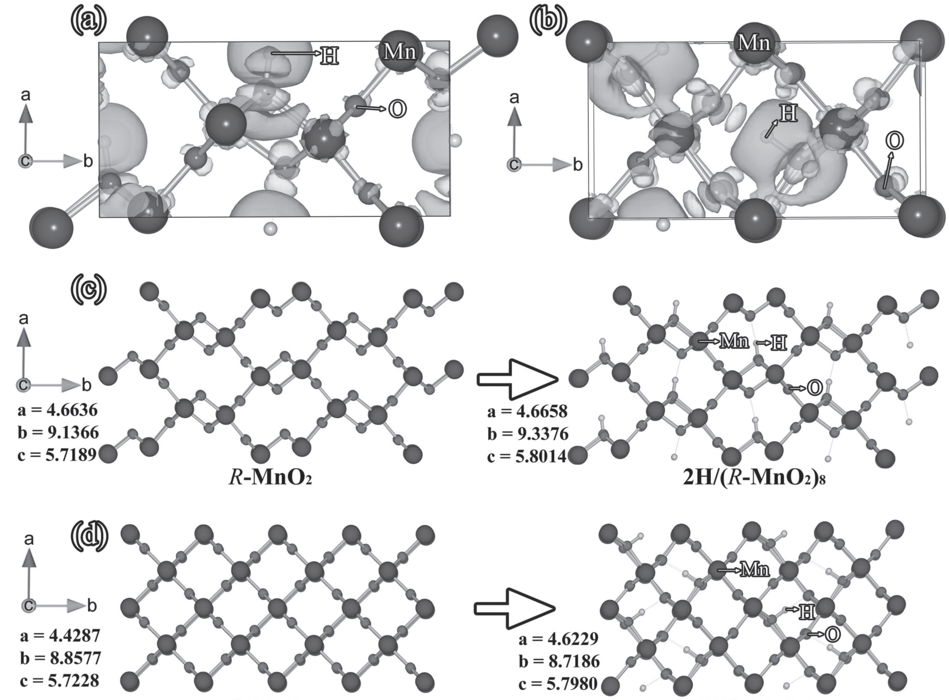

Figure 5. Electron density difference after proton intercalation in a) R-MnO_2 and b) β-MnO_2. The yellow and blue isosurfaces indicate the density change of +0.02 and –0.02 eÅ^{-3}– respectively. c) Change in atomic structure for R-MnO_2 and $2H/(R\text{-}MnO_2)_8$ model. d) Change in atomic structure for β-MnO_2 and $2H/(\beta\text{-}MnO_2)_8$ model.

and β-MnO_2, respectively. The yellow and blue isosurfaces indicate density change of +0.02 and –0.02 $e\text{Å}^{-3}$, compared to the pure MnO_2 and isolated H atoms, respectively. The density differences between proton and its first neighboring O atoms result in reduced electron density at the Mn–O bond, indicating that the bonds can be weakened after proton intercalation. This bond weakening, as confirmed again by the elongation of Mn-O distance from 1.9 to 2.0 Å, leads to the softening of MnO_2. Figure 5c presents the change in atomic structure of R-MnO_2, showing the proton intercalation induced lattice expansion of 2.20% along the b axis and 1.44% along the c axis in $2H/(R\text{-}MnO_2)_8$. The formation of covalent bond between the proton and the first neighboring pyramidal oxygen with an O-H distance of about 1 Å weakens Mn-O bonds. However, only a weak H-bond is formed due to the long distance of 2.1 Å from the proton to the pyramidal oxygen across the 2 × 1 tunnel (Figure 5c). Therefore, no obvious expansion can be found along the a axis. In the case of β-MnO_2 (Figure 5d), the inserted proton forms a covalent bond with an oxygen atom, at an O-H distance of 1.0 Å. Different from R-MnO_2, a strong hydrogen bond forms due to the shorter distance of 1.6 Å from the proton to the oxygen across the 1 × 1 tunnel of β-MnO_2. The lattice expands 4.38% along the a axis and 1.32% along the c axis in $2H/(\beta\text{-}MnO_2)_8$. However, a lattice contraction of 1.57% along b axis is found by the distortion of the 1 × 1 tunnel caused by the strong H-bond as well as the covalent bond (Figure 5b,d). The volume expansion of $2H/(\beta\text{-}MnO_2)_8$ and $2H/(R\text{-}MnO_2)_8$ are calculated to be 4.0% and 3.7%, respectively, which are larger than that measured by the in situ AFM in Figure 3. We interpret this difference as due to the self-accommodation of the expansion by localized compression of nanostructured MnO_2 film, as unveiled by in situ AFM observations (Figure 3). The 31.3% and 14.1% decrease in elastic modulus can also be found for $2H/(R\text{-}MnO_2)_8$ and $2H/(\beta\text{-}MnO_2)_8$, compared with pure counterparts, respectively. This trend is consistent with results obtained from indentation experiments. The proton intercalation induced decrease of nanoindentation hardness and Young's modulus must be favorable for the elastic deformation of MnO_2 during the discharging process.

3. Conclusions

In summary, we demonstrate, for the first time, the feasibility to explore the correlation between the energy storage performance and the microstructure of nanostructured film via dynamic observation of the growth and in situ probing the mechanical properties in aqueous electrolyte by using in situ AFM. The pulsed current deposited porous nanostructured γ-MnO_2 exhibits a high specific capacitance of 437 F/g and a remarkable cycling performance with >96% capacitance retention after 10 000 cycles. A series of dramatic evolutions of nanostructured MnO_2 film involving progressive nucleation, 3D growth, reversible expansion, proton intercalation induced softening, and self-accommodation phenomena, which have not been considered in the conventional fabrication method of nanostructured MnO_2, can be correlated to its remarkable energy storage performance. From the measurements, we also determined, for the first time, the Young's modulus and nanoindentation hardness of nanostructured MnO_2, which are important parameters for designing advanced electrochemical capacitors. The methodology described here should stimulate real-time studies of the microscopic processes in electrochemical capacitors and lead to a more complete understanding of the coupled physical-chemical mechanism governing electrochemical capacitor performance and reliability, especially microstructure-dependent properties. More generally, the in situ AFM in conjunction with in situ nanoindentation offers great potential for addressing many fundamental issues in materials science, chemistry, mechanics, biology, and other fields of science.

4. Experimental Section

Fabrication of Electrochemical Device: Supporting Information Figure S1a shows the schematic of the electrochemical device, which is composed of a platinum film as the counter electrode, Ag/AgCl microelectrode as the reference electrode, and ITO film as the conductive substrate for nanostructured MnO_2 films. The electrochemical measurement and electrodeposition were both performed with an electrochemical workstation. 0.1 M $Mn(NO_3)_2$ and 0.1 M $NaNO_3$ aqueous solution was used as the source components for in situ pulsed current electroplating of MnO_2. Supporting Information Figure S1b is the corresponding current waveform of pulse current deposition. During the sufficient off-time period (the net current density is zero), in situ atomic force microscopy (AFM) observations with tapping model were performed to avoid surface damage. A small current density of 5×10^{-5} A/cm^2 was used for the electrodeposition. After deposition, the cyclic voltammetric (CV) and electrochemical impedance spectroscopy (EIS) measurements were conducted using 1 M KCl aqueous electrolyte. CV tests were carried out in the voltage range of 0–0.8 V, and EIS tests were carried out in the frequency range of 0.1–10^4 Hz. Experimental results based on the microbalance revealed that the faraday current efficiency for deposition was 98.2%, which was used to calculate the mass of MnO_2.

Microscopic and Mechanical Characterization: The X-ray diffraction (XRD) patterns of the samples were observed by an X'Pert Pro diffractometer using Cu-Ka radiation (λ = 0.15418 nm). The microstructure of the samples was examined by transmission electron microscopy (TEM, FEI, Tecnai G2 F30). X-ray photoelectron spectroscopy (XPS) analysis was conducted using an Al Kα (1486.6 eV) monochromatic X-ray source (Axis Ultra DLD, Kratos). A Hysitron TI900 Triboindenter combined with a Dimension Edge AFM was used to perform imaging and in situ nanoindentation tests for mechanical property measurements.

First-Principles Calculations: The structure and elastic modulus were calculated using density functional theory formalism with generalized gradient approximation parameterized by Perdew and Wangusing planewave basis set.[47] The electron-ion interactions were described using the ultrasoft Vanderbilt-type pseudopotentials with $1s^1$, $2s^22p^4$, and $3d^54s^2$ as the valence electron configurations for the hydrogen, oxygen, and manganese, respectively.[48] A Broyden–Fletcher–Goldfarb–Shanno (BFGS) algorithm was applied to minimize the Kohn-Sham energy with plane-wave cutoff of 380 eV. All the calculations were fully optimized and were calculated with spin polarization. For the relaxion, the k-point sampling was set as 0.04 Å. The 1 × 2 × 2 supercell and 1 × 1 × 2 supercell were used for β-MnO_2 and R-MnO_2, respectively. This nanostructured MnO_2 film exhibited a specific capacitance of 437 F/g over the 0.8 V potential window, which can be translated to 350 C/g. EIS results revealed that the pseudofaradaic mechanism was absolute predominant in the energy storage process (Supporting Information Figure S6). About 0.3 H^+ per Mn atom is involved in the charge storage mechanism. Therefore, $2H/(MnO_2)_8$ models were selected for convenience. The proton were added to β-MnO_2 near a planar oxygen atom (see Figure 5d) and to R-MnO_2 near a pyramidal oxygen atom (see

Figure 5c), and the proton were placed as far away as possible to each other for $2H/(MnO_2)_8$ model. The elastic coefficients were determined by applying a set of given homogeneous deformations and calculating the resulting stress with respect to optimizing the internal degrees of freedoms, in which a 7 × 4 × 6 Monkhorst-Pack *k*-point mesh was used.[49]

Supporting Information

Supporting Information is available from the Wiley Online Library or from the author.

Acknowledgements

X.Y.T., J.D., Y.S., and S.L.Z., contributed equally to this work. This work was supported by the National Natural Science Foundation of China (51002138 and 51172205), the Natural Science Foundation of Zhejiang Province (Y4092023, Y4090420 and Y4110523), the Qianjiang Project of Zhejiang Province (2010R10029), the Scientific Research Foundation for the Returned Overseas Chinese Scholars (2010609) and New Century Excellent Talents in University (NCET 111079). Y.S. and X.D.L. acknowledge the support from the National Science Foundation (CMMI-1129979 and CMMI-0968843). The authors thank Professors Haiyan Xiao and Jianguo Wang for helpful discussions.

Received: January 29, 2013
Revised: March 9, 2013
Published online: April 19, 2013

---

[1] J. R. Miller, P. Simon, *Science* **2008**, *321*, 651.
[2] J. Chmiola, C. Largeot, P. L. Taberna, P. Simon, Y. Gogotsi, *Science* **2010**, *328*, 480.
[3] Y. W. Zhu, S. Murali, M. D. Stoller, K. J. Ganesh, W. W. Cai, P. J. Ferreira, A. Pirkle, R. M. Wallace, K. A. Cychosz, M. Thommes, D. Su, E. A. Stach, R. S. Ruoff, *Science* **2011**, *332*, 1537.
[4] H. Jiang, J. Ma, C. Z. Li, *Adv. Mater.* **2012**, *24*, 4197.
[5] L. H. Bao, X. D. Li, *Adv. Mater.* **2012**, *24*, 3246.
[6] X. Y. Lang, A. Hirata, T. Fujita, M. W. Chen, *Nat. Nanotechnol.* **2011**, *6*, 232.
[7] T. Brezesinski, J. Wang, S. H. Tolbert, B. Dunn, *Nat. Mater.* **2010**, *9*, 146.
[8] H. Y. Lee, J. B. Goodenough, *J. Solid State Chem.* **1999**, *144*, 220.
[9] M. Toupin, T. Brousse, D. Belanger, *Chem. Mater.* **2004**, *16*, 3184.
[10] W. Chen, R. B. Rakhi, L. B. Hu, X. Xie, Y. Cui, H. N. Alshareef, *Nano Lett.* **2011**, *11*, 5165.
[11] L. Y. Yuan, X. H. Lu, X. Xiao, T. Zhai, J. J. Dai, F. C. Zhang, B. Hu, X. Wang, L. Gong, J. Chen, C. G. Hu, Y. X. Tong, J. Zhou, Z. L. Wang, *ACS Nano* **2012**, *6*, 656.
[12] X. H. Lu, T. Zhai, X. H. Zhang, Y. Q. Shen, L. Y. Yuan, B. Hu, L. Gong, J. Chen, Y. H. Gao, J. Zhou, Y. X. Tong, Z. L. Wang, *Adv. Mater.* **2012**, *24*, 938.
[13] X. H. Lu, G. M. Wang, T. Zhai, M. H. Yu, J. Y. Gan, Y. X. Tong, Y. Li, *Nano Lett.* **2012**, *12*, 1690.
[14] G. H. Yu, L. B. Hu, M. Vosgueritchian, H. L. Wang, X. Xie, J. R. McDonough, X. Cui, Y. Cui, Z. N. Bao, *Nano Lett.* **2011**, *11*, 2905.
[15] G. H. Yu, L. B. Hu, N. A. Liu, H. L. Wang, M. Vosgueritchian, Y. Yang, Y. Cui, Z. A. Bao, *Nano Lett.* **2011**, *11*, 4438.
[16] R. Liu, J. Duay, S. B. Lee, *ACS Nano* **2011**, *5*, 5608.
[17] H. W. Shim, A. H. Lim, K. M. Min, D. W. Kim, *CrystEngComm* **2011**, *13*, 6747.
[18] L. B. Hu, W. Chen, X. Xie, N. A. Liu, Y. Yang, H. Wu, Y. Yao, M. Pasta, H. N. Alshareef, Y. Cui, *ACS Nano* **2011**, *5*, 8904.
[19] M. J. Deng, J. K. Chang, C. C. Wang, K. W. Chen, C. M. Lin, M. T. Tang, J. M. Chen, K. T. Lu, *Energy Environ. Sci.* **2011**, *4*, 3942.
[20] L. H. Bao, J. F. Zang, X. D. Li, *Nano Lett.* **2011**, *11*, 1215.
[21] J. A. Yan, E. Khoo, A. Sumboja, P. S. Lee, *ACS Nano* **2010**, *4*, 4247.
[22] Z. S. Wu, W. C. Ren, D. W. Wang, F. Li, B. L. Liu, H. M. Cheng, *ACS Nano* **2010**, *4*, 5835.
[23] S. W. Lee, J. Kim, S. Chen, P. T. Hammond, Y. Shao-Horn, *ACS Nano* **2010**, *4*, 3889.
[24] Y. Hou, Y. W. Cheng, T. Hobson, J. Liu, *Nano Lett.* **2010**, *10*, 2727.
[25] S. Chen, J. W. Zhu, X. D. Wu, Q. F. Han, X. Wang, *ACS Nano* **2010**, *4*, 2822.
[26] H. Zhang, G. P. Cao, Z. Y. Wang, Y. S. Yang, Z. J. Shi, Z. N. Gu, *Nano Lett.* **2008**, *8*, 2664.
[27] R. Liu, S. B. Lee, *J. Am. Chem. Soc.* **2008**, *130*, 2942.
[28] A. E. Fischer, K. A. Pettigrew, D. R. Rolison, R. M. Stroud, J. W. Long, *Nano Lett.* **2007**, *7*, 281.
[29] C. C. Hu, T. W. Tsou, *Electrochem. Commun.* **2002**, *4*, 105.
[30] J. P. Liu, J. Jiang, C. W. Cheng, H. X. Li, J. X. Zhang, H. Gong, H. J. Fan, *Adv. Mater.* **2011**, *23*, 2076.
[31] A. Cross, A. Morel, A. Cormie, T. Hollenkamp, S. Donne, *J. Power Sources* **2011**, *196*, 7847.
[32] K. W. Nam, M. G. Kim, K. B. Kim, *J. Phys. Chem. C* **2007**, *111*, 749.
[33] H. M. Zheng, R. K. Smith, Y. W. Jun, C. Kisielowski, U. Dahmen, A. P. Alivisatos, *Science* **2009**, *324*, 1309.
[34] H. G. Liao, L. K. Cui, S. Whitelam, H. M. Zheng, *Science* **2012**, *336*, 1011.
[35] N. de Jonge, F. M. Ross, *Nat. Nanotechnol.* **2011**, *6*, 695.
[36] J. Y. Huang, L. Zhong, C. M. Wang, J. P. Sullivan, W. Xu, L. Q. Zhang, S. X. Mao, N. S. Hudak, X. H. Liu, A. Subramanian, H. Y. Fan, L. A. Qi, A. Kushima, J. Li, *Science* **2010**, *330*, 1515.
[37] S. K. Jeong, M. Inaba, R. Mogi, Y. Iriyama, T. Abe, Z. Ogumi, *Langmuir* **2001**, *17*, 8281.
[38] C. C. Hu, T. W. Tsou, *J. Power Sources* **2003**, *115*, 179.
[39] S. Nijjer, J. Thonstad, G. M. Haarberg, *Electrochim. Acta* **2000**, *46*, 395.
[40] B. Babakhani, D. G. Ivey, *J. Power Sources* **2011**, *196*, 10762.
[41] P. C. Chen, G. Z. Shen, Y. Shi, H. T. Chen, C. W. Zhou, *ACS Nano* **2010**, *4*, 4403.
[42] X. Y. Tao, J. Liu, G. Koley, X. D. Li, *Adv. Mater.* **2008**, *20*, 4091.
[43] X. D. Li, H. S. Gao, C. J. Murphy, K. K. Caswell, *Nano Lett.* **2003**, *3*, 1495.
[44] X. D. Li, W. C. Chang, Y. J. Chao, R. Z. Wang, M. Chang, *Nano Lett.* **2004**, *4*, 613.
[45] Y. Chabre, J. Pannetier, *Prog. Solid State Chem.* **1995**, *23*, 1.
[46] D. Balachandran, D. Morgan, G. Ceder, *J. Solid State Chem.* **2002**, *166*, 91.
[47] J. P. Perdew, K. Burke, M. Ernzerhof, *Phys. Rev. Lett.* **1997**, *78*, 1396.
[48] D. Vanderbilt, *Phys. Rev. B* **1990**, *41*, 7892.
[49] R. A. Evarestov, V. P. Smirnov, *Phys. Rev. B* **2004**, *70* , 233101.